Impact of Microstructure on the Electron-hole Interaction in Metal Halide Perovskites

Arman Mahboubi Soufiani[1†], Zhuo Yang[2†], Trevor Young[1], Atsuhiko Miyata[2], Alessandro Surrente[2],

Alexander Pascoe[3], Krzysztof Galkowski[2,4], Mojtaba Abdi-Jalebi[5], Roberto Brenes[6], Joanna Urban[2],

Nan Zhang[2], Vladimir Bulović[5], Oliver Portugall[2], Yi-Bing Cheng[3], Robin J. Nicholas[7],

Anita Ho-Baillie[1*], Martin A. Green[1], Paulina Plochocka[2*], Samuel D. Stranks[5,6*]

[1]Australian Centre for Advanced Photovoltaics,
School of Photovoltaic and Renewable Energy Engineering,
University of New South Wales, Sydney, NSW 2052, Australia

[2]Laboratoire National des Champs Magnétiques Intenses, CNRS-UGA-UPS-INSA, 143
Avenue de Rangueil, 31400 Toulouse, France

[3]Department of Materials Science and Engineering, Monash University, Clayton, Vic 3800, Australia

[4]Institute of Experimental Physics, University of Warsaw - Pasteura 5, 02-093 Warsaw, Poland

[5]Cavendish Laboratory, University of Cambridge, J. J. Thomson Avenue, Cambridge CB3 0HE,
United Kingdom

[6]Research Laboratory of Electronics, Massachusetts Institute of Technology, Cambridge, MA 02139,
United States

[7]Clarendon Laboratory, University of Oxford, Parks Road, Oxford OX1 3PU, United Kingdom

[†] These authors contributed equally to this work.

[*]e-mail:
sds65@cam.ac.uk
paulina.plochocka@lncmi.cnrs.fr
a.ho-baillie@unsw.edu.au

1

Abstract

Despite the remarkable progress in the performance of devices based on the metal halide perovskite semiconductor family, there is still a lack of consensus on their fundamental photophysical properties. Here, using magneto-optical transmission spectroscopy we elucidate the impact of the microstructure on the Coulomb interaction between photo-created electron-hole pairs in methylammonium lead triiodide (MAPbI$_3$) and the triple-cation lead mixed-halide composition, Cs$_{0.05}$(MA$_{0.17}$FA$_{0.83}$)$_{0.95}$Pb(I$_{0.83}$Br$_{0.17}$)$_3$ (Cs: Cesium, MA: methylammonium, FA: formamidinium) by investigating thin films with a wide range of grain sizes from tens of nanometers to microns. At low temperatures, in which thermal fluctuations of the interactions are frozen and the rotational disorder of the organic cation is negligible, the exciton binding energy and reduced effective mass of carriers remain effectively unchanged with grain size. We conclude that the microstructure plays a negligible role in the Coulomb interaction of the photo-created electron-hole pairs, in contrast to previous reports. This renewed understanding of the relationship between these fundamental electronic properties and the microstructure is critical for future fundamental studies and improving device design.

Key words: hybrid perovskites, microstructure, exciton binding energy, excitonic reduced effective mass, magneto-optical spectroscopy

Broader context:

Metal halide perovskites such as methylammonium lead iodide (CH$_3$NH$_3$PbI$_3$) and alloyed mixed-cation lead mixed-halide counterparts such as Cs$_{0.05}$(MA$_{0.17}$FA$_{0.83}$)$_{0.95}$Pb(I$_{0.83}$Br$_{0.17}$)$_3$ are creating enormous excitement for their use in high-performance solar cells with potential for exceptionally low capital-intensity for production. An important parameter that dictates the design of a solar cell is the strength of the Coulomb interaction between the photo-generated electron in the conduction band and the hole in the valence band (i.e. the exciton binding

49 energy). Recently, it has been suggested that the exciton binding energy of the perovskite

50 material is influenced by the size of the grains of the perovskite film, and therefore different

51 device design will be required depending on the grain size. Here, we perform magneto-optic

52 measurements on films with different grain sizes to directly show that the microstructure has a

53 negligible influence on the excitonic properties in the samples, and that excitons do not play a

54 significant role in films with any of the polycrystalline morphologies studied. This means that

55 excitons should not be factor for the design of optoelectronic devices based on polycrystalline

56 $CH_3NH_3PbI_3$ and similar materials with different grain sizes, making future device

57 architecture optimisation less constrained.

58 **Introduction**

59 Solar cells based on lead halide perovskites (with general chemical formula of ABX_3; A =

60 $CH_3NH_3^+$, $HC(NH_2)_2^+$ or Cs^+; B = Pb^{2+} ; X = I^-, Br^- or Cl^-) have achieved astonishingly high

61 power conversion efficiencies exceeding 22% in only seven years since they were first used as

62 sensitizers in photovoltaic solar cells [1-3]. Since then, the remarkable properties of these

63 crystalline semiconductors, such as the tunability of their optoelectronic properties through

64 fabrication of layers with different morphologies, compositions and crystal qualities [4-7], have

65 been further exploited to develop a variety of promising optoelectronic devices [8-11].

66 As for any emerging semiconductor material deployable in optoelectronic devices, the

67 strength of the Coulomb interaction between the photo-generated electron in the conduction

68 band and the hole in the valence band is of high importance. This was a focus of several

69 studies on perovskites about two decades ago [12-14] and has recently regained attention [15-18]

70 mainly due to the promising outlook of perovskites for solar photovoltaics [10], light-emitting

71 diodes [11] and lasing applications [19] with polycrystalline thin films and single crystals of

72 superior quality than those synthesized two decades ago.

73 The latest studies have come to a consensus that the exciton binding energy – alternatively

74 known as effective Rydberg (Ry^*) in the Wannier-Mott exciton model – of well-studied

75 $CH_3NH_3PbI_3$ and $CH_3NH_3PbBr_3$ polycrystalline thin films is ~5-12 meV [15, 17, 18] and ~25 meV

76 [16, 18] in the room temperature phase, respectively. These low values, with respect to thermal

77 energy at room temperature ($k_b \times T \approx 26$ meV; k_b is the Boltzmann constant and T is the

78 temperature in Kelvin), are due to generally weak many-body effects (i.e. Coulombic

79 interactions) in these semiconductor systems [20]. Nevertheless, there is ongoing debate

80 concerning the possible tunability of this parameter with variations of the microstructure and

81 hence crystal quality of the perovskite layer [21, 22], being speculated to influence the photo-

82 excited exciton binding energies.

83 It has been proposed that disordered organic cation dipole domains in small and defective

84 crystals with a large portion of poly-crystallinity can create a large electrostatic potential

85 fluctuation which causes a substantial screening of the photo-generated excitons [22]. This could

86 lead to a very small value of Ry^* on the order of ~2-5 meV [23, 24] meaning that the material

87 behaves as if in the non-excitonic regime. On the other hand, large and defect-free crystals can

88 exhibit an order of magnitude greater values of Ry^* [22, 25]. As a result, one current hypothesis is

89 that it is not possible to assign a universal value to the exciton binding energy of the

90 commonly used $CH_3NH_3PbI_3$ hybrid lead halide perovskites.

91 A key consequence of this hypothesis could be a change in the working regime (i.e. photo-

92 excited carrier dissociation and transport) of solar cells fabricated from active layers with

93 diverse microstructures. Knowledge of the value of the exciton binding energy is essential

94 because it determines the nature of the majority of the photo-generated species (i.e. free

95 carriers versus excitons) in a semiconductor. For devices comprised of materials with binding

96 energies greater than the probability of thermal dissociation at the working temperature, there

97 would need to be an additional mechanism for exciton dissociation into free carriers, such as

4

98   an additional heterojunction, through which they can readily contribute to the photocurrent [26].

99   In the case that the binding energies are so low that the fraction of photo-excited species that

100   are excitons is negligible, the n- and p-type contacts in the heterojunction structure of the solar

101   cell (cf. most perovskite solar cells) would simply act as charge-selective contacts for the

102   photo-generated electrons and holes, respectively, facilitating simpler device designs.

103   Altogether, these points highlight the need to fully understand the exciton-morphology

104   relationship.

105   Here, we elucidate the influence of the microstructure, manipulated through the perovskite

106   fabrication method, on the exciton binding energy Ry^* and the excitonic reduced mass (μ) for

107   a variety of $CH_3NH_3PbI_3$ crystal sizes covering the size range reported in devices to date. The

108   impact of the local order and the degree of poly-crystallinity on electron-hole interaction is

109   unraveled through a direct measurement of Ry^* and μ for thin films with different grain sizes.

110   These measurements are performed at low temperature (2 K) at which the impact of $CH_3NH_3^+$

111   thermal orientational dynamic rearrangement is mitigated. We provide strong evidence that

112   the grain size has negligible influence on the exciton binding energy and effective mass in

113   $CH_3NH_3PbI_3$ and, thus, does not affect the dissociation probability of the bulk excitons and

114   their stability in the photo-excited charge carrier population.

115   **Results and Discussion**

116   *Sample Morphology*

117   A wide range of fabrication methods, from single-step [27] to sequential deposition [28] and

118   solution-processed [29] to vapor-assisted [30] techniques, have been employed to fabricate the

119   active layer of perovskite optoelectronic devices in the literature. Here, different deposition

120   methods, which have been shown to give corresponding high-performance solar cells with

121   efficiencies of >16 % [6, 31, 32], are used to controllably tune the perovskite grain size in the

films. These samples with $CH_3NH_3PbI_3$ chemical composition but fabricated via different methods with various resulting morphologies simulate the range of different degrees of structural disorder and poly-crystallinity in the $CH_3NH_3PbI_3$ layer in high-performance perovskite devices fabricated to date [22]. The top-view scanning electron microscope (SEM) images of the samples are presented in **Figure 1A-D**. The morphologies vary from a planar polycrystalline film with grain sizes of 772±227 nm [32] (**A**; large grain polycrystalline annotated **LPC**) and polycrystalline film with grain sizes of 214±57 nm [31] (**B**; small grain polycrystalline annotated **SPC**), to small crystals of 291±64 nm fabricated by a two-step dipping technique [6] (**C**; annotated **SC**) and also perovskite infiltrated into a ~2 µm thick mesoporous Aluminum oxide scaffold (mp-Al_2O_3) with grain sizes of <50 nm (**D**; annotated **MP**). As can be seen in the top-view SEM image of the **MP** sample, there is no visible capping layer formed on top of the mesoscopic phase and, therefore, a potential artefact from the larger grain sizes of a capping layer does not influence the related data analysis.

Magneto-optical Transmission Measurements

Studying the optical behavior of excitons under external fields has proven to be a powerful tool to reveal properties of these quasi-particles in semiconductors [33]. Here, we conducted optical transmission measurements under high magnetic fields (*B*) up to 70T on the samples presented in **Figure 1**. Typical transmission spectra for the large grain polycrystalline thin film sample, showing a strong 1s excitonic transition, are given in **Figure 2A**. For unambiguous identification of the weaker optical transitions, we show in **Figure 2B** the ratio of the transmission spectrum at a specific high magnetic field over the transmission spectrum taken at zero field, illustrating the free-carrier transitions. In **Figure 2C** we show transmission measurements at several monochromatic probe energies under very high magnetic field (<150T) achieved using a short pulse technique. The related spectra for other morphologies are provided in the Supplementary Information, **Figures S1-S3**.

147   We note that a hydrogen-like excitonic behavior [34] can be assumed for $CH_3NH_3PbI_3$ in the

148   low-temperature orthorhombic phase. The strong minimum in the transmission spectra

149   (**Figure 2A**), attributed to the 1s state of the hydrogen-like free exciton [17], blue shifts with

150   increase of the magnetic field. The second minimum, located at slightly higher energies than

151   the 1s state, is attributed to the first excitonic excited state (labelled as 2s in **Figure 2A)** and

152   also exhibits a blue-shift with magnetic field.

153   The Landau levels, the free carrier states with quantum numbers $N=0,1,2,\ldots$ formed by

154   quantization of the particle's motion in the plane perpendicular to the magnetic field [33], can be

155   observed at higher energies in the strong magnetic field regime in which $\hbar\omega_c >> Ry^*$ (

156    $\hbar\omega_c = \hbar eB/\mu$), where $\hbar$ and e are Planck's constant and the electron charge, respectively, ω_c is

157   the cyclotron frequency, and $\mu^{-1} = m_e^{-1} + m_h^{-1}$ is the reduced mass of the exciton (m_e and m_h are

158   electron and hole masses, respectively). The free carrier Landau level transitions are dominant

159   at high magnetic fields with transition energy described by $E(B) = E_g + (N+1/2)\hbar\omega_c$ [16, 17]

160   where E_g is the bandgap. We can then fit the measured optical transitions between Landau

161   levels to extract the reduced mass, μ, independent of the exciton binding energy. The value of

162   the reduced mass thus obtained is used as a fixed parameter in the fit of the hydrogen-like

163   excitonic transitions to extract the exciton binding energy, based on a model which describes

164   the hydrogen atoms in high magnetic field [35]. In this model, a dimensionless parameter γ

165   which is defined as $\gamma = \hbar\omega_c/2Ry^*$ is used. Makado and McGill calculated the transition

166   energies of excitonic states $E_n(\gamma)$ as a function of quantum number n up to 4 and γ ranging

167   from 0 to 10 [35]. Given values of the magnetic field B and the reduced mass μ, the binding

168   energy Ry^* is the only fitting parameter for the full set of hydrogenic transitions.

169 The complete set of these excitonic and free carrier transition energies for the **LPC** sample is

170 plotted in the fan diagram in **Figure 2D**. The observation of many Landau levels in the

171 magnetic field <150T allows precise determination of the reduced mass. Knowledge of the

172 reduced mass in turn imposes strong constraints on fitting the excitonic binding energy. An

173 additional influential constraint on the value of the binding energy is set if the higher

174 excitonic transition resonances such as the 2s state are resolved, as for the **LPC** morphology.

175 The observation of a well-resolved 2s state at intermediate magnetic field fixes the transition

176 energy of 2s at zero magnetic field using the model described earlier. The energy separation

177 of 1s-2s at zero magnetic field follows the series of 3D hydrogen-like energy states,

178 $E_n = E_g - Ry^*/n^2$ where E_n is the excitonic transition energy at zero magnetic field. This

179 gives a strong constraint on the exciton binding energy.

180 The fitting to the hydrogen-like excitonic (dashed lines) and free carrier (solid lines)

181 transitions, as explained in detail in refs. [16, 17, 35], is presented in **Figure 2D** and the Ry^* and μ

182 values for the **LPC** sample are calculated to be 16±1 meV and 0.102±0.002 m_0, respectively.

183 For the morphologies other than **LPC** (i.e. **SPC**, **SC** and **MP**), the identification of free carrier

184 transitions at high energies allows us to obtain the values of the the reduced masses. The

185 extracted μ values are presented in **Table 1** and are very close to the value originally reported

186 by Miyata *et al.* ($\mu = 0.104±0.003$ m_0) [17]. Importantly, we find that the microstructure has

187 negligible influence on the reduced mass. This indicates that the polaron coupling contant,

188 incorporating the effective longitudinal optical (LO) phonon energy and the optical and static

189 dielectric constants of the medium, which couples to the band-edge bare effective masses to

190 form the polaronic masses [18, 36], is only minimally influenced by the variation in

191 microstructure.

192　In the absence of a clear observation of the 2s excitonic transitions for the **SPC**, **SC** and **MP**

193　samples, the global fit to the full excitonic and free-carrier transitions was employed and the

194　resulting unchanged Ry^* values are presented in **Table 1**. To visualize the negligible change in

195　the optical response under external magnetic fields of the $CH_3NH_3PbI_3$ films with different

196　morphology, the overlaid fan diagrams of the complete set of excitonic and free carrier optical

197　transitions after shifting by the corresponding bandgap offsets are presented in **Figure 3(A)**.

198　Here we clearly show that these $CH_3NH_3PbI_3$ samples, although composed of dramatically

199　different grain sizes and morphologies, exhibit similar magneto-optical behaviour.

200　Furthermore, the XRD patterns (**Figure S4)** show that the $CH_3NH_3PbI_3$ **SPC** and **SC** thin

201　films have some PbI_2 impurities, indicating that the presence of small amounts of PbI_2 also

202　does not affect the excitonic properties of perovskites. We also note that, although the changes

203　in the grain size and morphology do not influence the low-temperature excitonic properties of

204　perovskites, they can affect the optoelectronic response of these materials including their PL

205　behaviour and the fraction of retained tetragonal phase within the orthorhombic phase upon

206　lowering the temperature [37-39].

207　It was recently shown that when replacing $CH_3NH_3^+$ by a larger monovalent organic cation,

208　formamidinium ($HC(NH_2)_2^+$), the excitonic characteristics of the corresponding perovskite,

209　Ry^* and μ, decreased by less than 15 % [16]. The larger steric size of formamidinium compared

210　to methylammonium results in a larger equatorial bond angle (lead-iodide-lead) and, thus, a

211　narrower optical bandgap [40]. The variation of the crystal size would result in a modified

212　interplay between the organic and the inorganic moieties in the perovskite structure, which in

213　turn changes the strain induced on the crystal structure and thus, impacts the bandgap. The

214　negligible impact on the excitonic characteristics of the degree of dipolar cation order and

215　structural arrangement induced by the variation of perovskite microstructure might be

216　analogous to the small impact of cation substitution on the excitonic properties, with the lead-

217 halogen sub-unit remaining unchanged in both cases. This indeed demonstrates the critical

218 role of the electronic properties of the inorganic cage in the determination of the excitonic

219 binding energy and reduced effective mass of perovskites. Moreover, this important

220 observation agrees with the recent work by Perez-Osorio *et al.* in which the largest

221 contribution to the static dielectric constant of $CH_3NH_3PbI_3$ was demonstrated to originate

222 from the stretching and rocking vibrational modes of the lead-halogen system rather than the

223 internal modes of the organic cation [41].

224 Using the values obtained for the effective dielectric constant ($\varepsilon = \sqrt{Ry^H \times \mu / Ry^* \times m_0}$,

225 where Ry^H = 13.6 eV is the Rydberg constant of the hydrogen atom) and the reduced mass, the

226 Bohr radius of the bound electron-hole system can be calculated. This is similar for all the

227 $CH_3NH_3PbI_3$ perovskite morphologies and is about 5 nm in the low temperature phase. The

228 Bohr radius is substantially smaller even than the perovskite crystal size of the **MP** sample

229 and it is consistent with the absence of any signature of a quantum confinement effect on the

230 optical transition of the corresponding excitons in the mesoscopic phase.

231 The correct interpretation of the optical absorption spectrum for the exciton binding energy

232 derivation in the room temperature tetragonal phase of $CH_3NH_3PbI_3$ (> 160 K) becomes more

233 difficult than in the orthorhombic phase as the large spectral broadening at higher

234 temperatures in the tetragonal phase can potentially mask critical optical transition features

235 even under high magnetic fields [17]. The increased broadening is most likely due to a

236 thermally-induced increase in the orientational disorder and rotational dynamics of the

237 unlocked organic cation above the structural phase transition [42]. The excitonic binding energy

238 has been reported in the literature [17, 18, 24, 43] to decrease upon orthorhombic-to-tetragonal

239 phase transition with a likely reason to be the slight increase in the dielectric constant of the

240 medium, which is in turn linked to the increase in the effective phonon energy coupling to the

241 carriers.

242 We argue that the change in the binding energy at the transition to the tetragonal phase for all

243 the morphologies investigated in this study would be similar. This can be partly understood by

244 the dominant influence of thermal disorder on the electrostatic fluctuations at room

245 temperature over the degree of poly-crystallinity and molecular order which are dominant at

246 lower temperatures [22]; the latter properties we have already shown above to have insignificant

247 impact on the electron-hole interaction. This is further supported by a recent theoretical study

248 by Motta *et al.* in which the impact of the degree of molecular dipole orientational disorder –

249 which could be induced by the grain size variation – on the binding energy in the high

250 temperature phase of $CH_3NH_3PbI_3$ was found to be only ~10 % [44].

251 To generalise our findings for $CH_3NH_3PbI_3$ to other perovskite compositions, we repeat the

252 measurements on a state-of-the-art triple-cation lead mixed-halide perovskite,

253 $Cs_{0.05}(MA_{0.17}FA_{0.83})_{0.95}Pb(I_{0.83}Br_{0.17})_3$ [2]. We consider two significantly different morphologies

254 of this perovskite composition, namely a planar polycrystalline thin film and a film with the

255 perovskite infiltrated into a thick mp-Al_2O_3 scaffold (corresponding SEM images are shown

256 in **Figure S5**). We show in **Figure S6** that both morphologies exhibit similar magneto-optical

257 responses and, thus, similar fundamental excitonic properties, with the binding energy and

258 reduced mass of 13±2 meV and 0.096±0.008 m_0, respectively (see **Table S1**). These results

259 allow us to extend our conclusions to the wider alloyed perovskite family, providing strong

260 evidence that the microstructure has a negligible impact on the excitonic properties in metal

261 halide perovskites.

262 Recently, Petrozza and co-workers used temperature-dependent time-resolved transient

263 absorption (TA) spectroscopy to track the fate of excitons following photo-excitation and to

264 understand the relationship between the excitonic properties and film morphology [22]. The

265 conclusion from this study was that the exciton binding energy and, therefore, exciton

266 stability can vary depending on the perovskite film microstructure in the tetragonal phase

267 which is most critical to solar cell operation. Their interpretation was based on the emergence

268 and evolution of the negative feature located at the high-energy end of the photobleach

269 signature in the transmission-difference spectrum, which was attributed to self-

270 renormalization of the exciton energy due to a change in its concentration upon decrease in

271 temperature and/or grain size variation. We note that the negative feature developing in the

272 high-energy tail of the TA spectra over time has been proposed to be primarily a consequence

273 of a bandgap renormalization effect (bandgap narrowing) and of a free carrier absorption,

274 among other possible mechanisms [45, 46]. The spectral TA analysis used in ref. [22], which is an

275 indirect technique for characterising excitonic properties, can also be influenced by

276 recombination mechanisms which are strongly influenced by the perovskite crystal

277 morphology. Furthermore, we note from a previous report for $CH_3NH_3PbBr_3$ perovskite that

278 while Ry^* probably remains unchanged by increasing the temperature from 2 K to room

279 temperature, the increase in the broadening of the linear absorption spectra lessens the 1s

280 transition strength [18, 47]. Although this spectral broadening increase is mainly attributed to

281 thermally-activated mechanisms, a change in the intrinsic broadening of perovskites with

282 different microstructures, due for instance to the difference in their inherent structural

283 disorder, can similarly influence the spectral shape while Ry^* remains unchanged. This makes

284 unambiguous interpretation of the linear and transient absorption spectra difficult when

285 relying on the detection and the strength of the excitonic feature – at the absorption edge – as

286 these techniques are indirect approaches for Ry^* determination compared to the direct

287 approach employed in this study (see **Figure S7** for the zero-field transmission spectra of the

288 four different $CH_3NH_3PbI_3$ morphologies). We note that it is possible there are also transient

289 changes in excitonic populations and properties (e.g. due to dynamic photo-excited changes in

290 dielectric constant) that will be averaged out in our steady-state measurements.

291 **Conclusions**

292 We investigated the relationship between the excitonic properties and microstructure of the

293 $CH_3NH_3PbI_3$ and $Cs_{0.05}(MA_{0.17}FA_{0.83})_{0.95}Pb(I_{0.83}Br_{0.17})_3$ perovskites using magneto-optical

294 spectroscopy measurements. We find that the microstructure does not influence the excitonic

295 binding energy of $CH_3NH_3PbI_3$ or the broader range of mixed-cation and mixed-halide

296 alloyed compositions. Thus, we conclude that excitons truly play a negligible role in the

297 operation of mixed organic-inorganic metal halide-based perovskites regardless of the thin

298 film deposition technique and final morphology, and that excitons need not be a factor for the

299 design of optoelectronic devices based on polycrystalline $CH_3NH_3PbI_3$ and similar materials

300 with different grain sizes. The universal values of ~16 meV and 0.102-0.109 m_0 for the

301 exciton binding energy and reduced effective mass in the low-temperature phase of

302 $CH_3NH_3PbI_3$ can be used as guidelines for interpretation of the spectroscopic data such as the

303 complex spectra of transient absorption measurements. It also implies that the electronic

304 structure of the inorganic cage – $(PbI_3)^-$ in the case of $CH_3NH_3PbI_3$ – is likely to have the

305 greatest contribution to the excitonic properties of organic-inorganic lead halide perovskites

306 rather than the degree of poly-crystallinity and the order of dipolar organic cation domains.

307

Figures

309
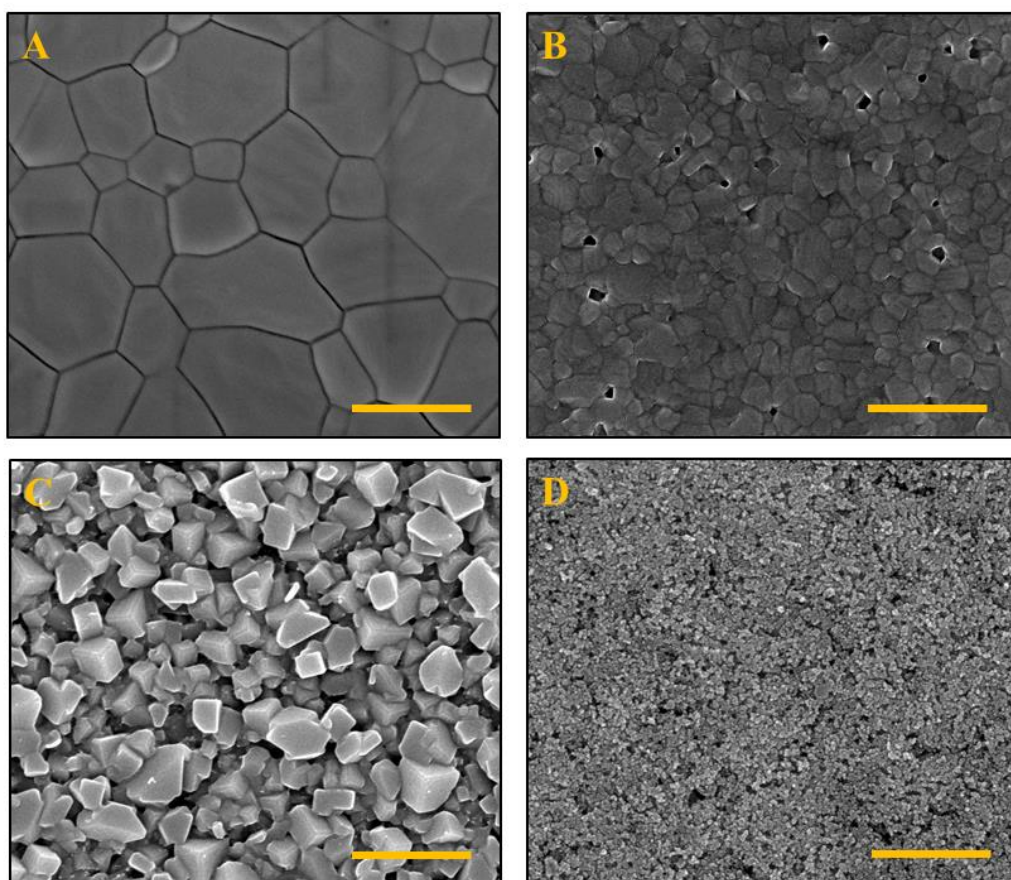
Figure 1 Morphology of CH₃NH₃PbI₃ samples. Top-view SEM images of $CH_3NH_3PbI_3$ layer with various morphologies fabricated on glass substrates. **A)** Polycrystalline thin film with grain sizes 772±227 nm (LPC). **B)** Polycrystalline thin film with grain sizes 214±57 nm (SPC). **C)** Small crystals of $CH_3NH_3PbI_3$ fabricated by the two-step solution-processed dipping technique, with resulting crystal sizes 291±64 nm (SC). **D)** $CH_3NH_3PbI_3$ infiltrated into a thick mesoporous-Al_2O_3 scaffold with grain sizes <50 nm (MP). Scale bars are 1 µm.
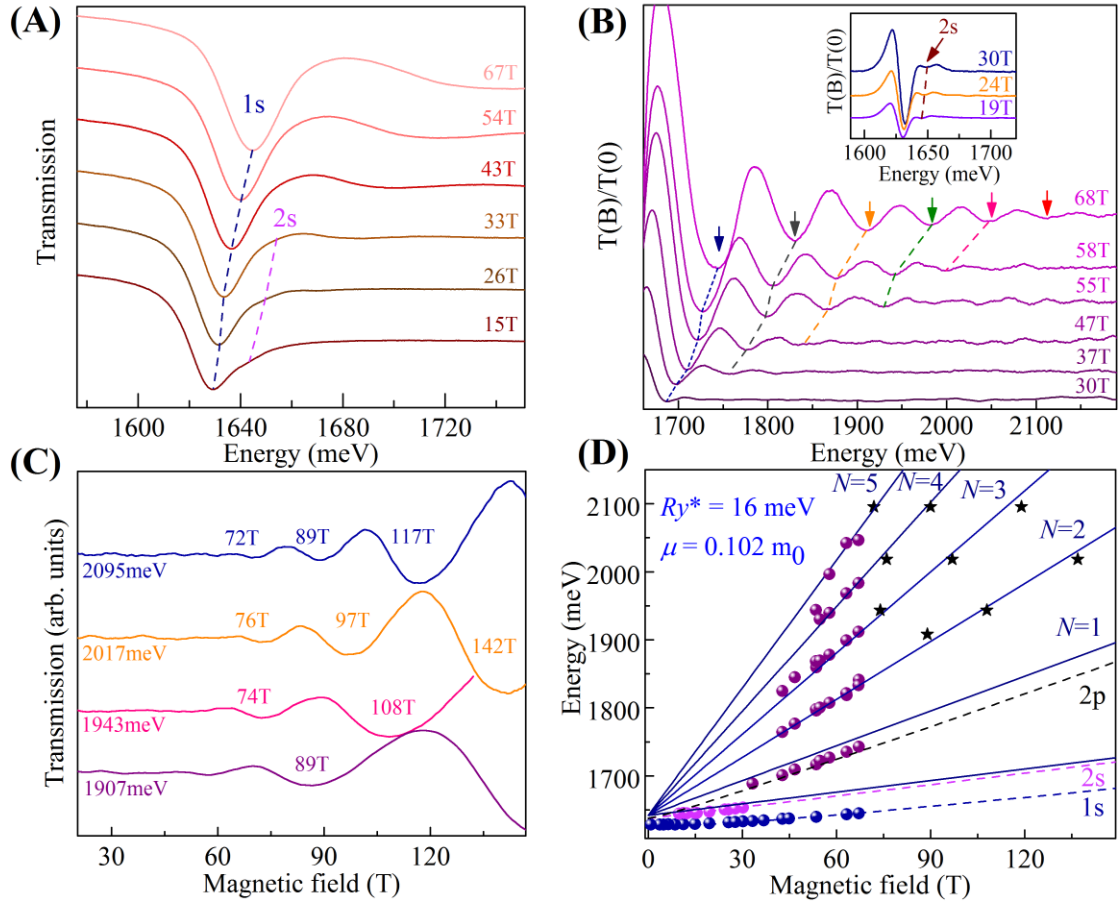
Figure 2 Magneto-optical transmission spectrum and fan chart measured at 2 K. A) Sequence of typical optical transmission spectra of the **LPC** sample measured at the indicated magnetic fields which show the 1s and 2s excitonic transitions with increased transmission. **B)** Sequences of the ratios of the transmission spectra in magnetic field $T(B)$ to that measured at zero field $T(0)$. The resonant absorption features of the free carrier Landau levels correspond to minima. **C)** Typical results of the low temperature monochromatic transmission as a function of magnetic field obtained by the short pulse technique. **D)** Fan chart of $CH_3NH_3PbI_3$ for the large grain polycrystalline sample. The circular data points are from long pulse field measurements and star symbol points are collected by short pulse mega-gauss measurements. The solid lines and the dashed lines are the fits to the set of Landau levels and the excitonic transitions, respectively.
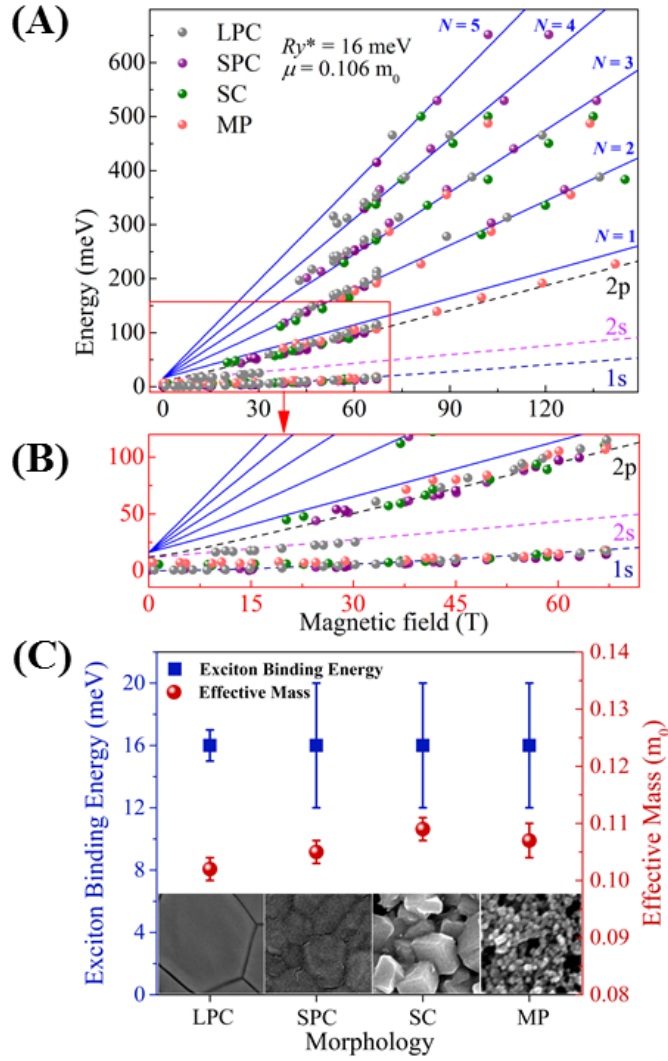
Figure 3 Comparison of the excitonic properties of the four different CH₃NH₃PbI₃ morphologies. A) Overlaid fan chart of the LPC, SPC, SC and MP samples. The solid lines and the dashed lines are the fits to the set of Landau levels and the excitonic transitions, respectively. **B)** The zoomed-in plot of the excitonic transitions region of the fan chart in panel **(A)**. **C)** The bottom panel illustrates the change in the Ry^* and μ for the various morphologies.

336   **Table 1** Summary of the parameters of the fits to the full Landau fan chart for the four different morphologies of

337    $CH_3NH_3PbI_3$ in the low temperature (2 K), orthorhombic phases. The figures in the brackets are the error

338   estimates of the parameters.

	Size Distribution (nm)	E_g (meV)	μ (m_0)	Ry^* (meV)
Large Polycrystalline	772(227)	1642(2)	0.102(0.002)	16(1)
Small Polycrystalline	214(57)	1643(2)	0.105(0.002)	16(4)
Small Crystal	291(64)	1639(2)	0.109(0.002)	16(4)
Mesoporous	<50	1638(2)	0.107(0.003)	16(4)

339

Acknowledgements

Author Contributions

AMS conceived the idea and designed the experiments with SDS and PP. TY, RB, AP and MA-J fabricated the samples. AMS, SDS and MA-J performed the SEM imaging and XRD measurements. The magneto-optic experiments were performed, under the supervsion of PP, by ZY, AM, AS, KG, JU and NZ, and the data analyzed by ZY. AH-B and MAG supervised AMS, Y-BC supervised AP, OP supervised AM, SDS supervised MA-J, SDS and VB supervised RB. AMS prepared the first draft of the manuscript with technical and editorial inputs from SDS, PP and RJN. All authors contributed to the final version of the manuscript.

Methods

CH₃NH₃PbI₃ Perovskite Sample preparation

Large grain polycrystalline film (LPC)

LPC perovskite films were prepared using a methylammonium iodide (CH_3NH_3I) and lead acetate $Pb(Ac)_2 \cdot 3H_2O$ precursor mixture[32]. To generate the perovskite solution, CH_3NH_3I (Dyesol) and $Pb(Ac)_2 \cdot 3H_2O$ were dissolved in anhydrous N,N-dimethylformamide at a 3:1 molar ratio with final concentration of 30 wt%, and the stabilizer hypophosphorous acid (HPA) was added at a molar ratio of 7.5% with respect to $Pb(Ac)2 \cdot 3H_2O$. $Pb(Ac)_2 \cdot 3H_2O$ (316512) and HPA (214906) were purchased from Sigma Aldrich. Microscope slides and coverslips were washed sequentially with soap (2% vol. Hellmanex in water), de-ionized water, isopropanol, acetone and finally treated under oxygen plasma for 10 min. The precursor solution was spin-coated at 2,000 r.p.m. for 45 s in a nitrogen-filled glovebox, and the substrates were then dried at room temperature for 10 min before annealing at 100 °C for 5 min. The samples were then stored in a nitrogen-filled glovebox until used.

Small grain polycrystalline film (SPC)

Soda-lime glass substrates 1 mm thick were purchased from J. Melvin Freed. The substrates were cleaned ultrasonically using soap solution (Helmanex), water, ethanol and iso-propanol for 15 minutes, each.

PbI_2 (99.99%) was purchased from Alfa Aesar and used without further purification. MAI was either synthesised in-house using a common method or else purchased from Dyesol. All the film preparation work was carried out under nitrogen atmosphere.

$CH_3NH_3PbI_3$ films were prepared by the "gas-assisted" method of Huang *et al.* [31]. A 25μL 45 wt% $CH_3NH_3PbI_3$ DMF solution, prepared from PbI_2 and CH_3NH_3I in a molar ratio of 1:1,

387   was spread on the substrate, on a spin-coater. An 80 L/min stream of nitrogen gas was blown

388   over the film during spinning at 6500 rpm, 2 s after the spinning commenced. The films were

389   annealed at 100°C on a hotplate for 10 min and then cooled to room temperature.

390   *Small crystal sample* **(SC)**

391   Soda-lime glass substrates treatment and precursor solution (PbI_2 and MAI) preparation were

392   similar to that of the small grain polycrystalline film.

393    $CH_3NH_3PbI_3$ films were prepared by the 2-step method of D'Innocenzo *et al.* [6]. The clean

394   glass substrates were heated on a hotplate at 70° C. A PbI_2 solution in DMF (462 mg/mL) was

395   warmed to 70°C and then spin-coated at 2000 rpm for 60 s. The PbI_2 films were subsequently

396   annealed at 70°C for 30 min. $CH_3NH_3PbI_3$ films with small crystal size were prepared by

397   dipping the PbI_2-coated substrates in a 0.044 M CH_3NH_3I solution in isopropanol at 25°C for

398   2 minutes. Samples were finally rinsed in anhydrous IPA to remove unreacted CH_3NH_3I.

399   *Mesoporous Al_2O_3* **(MP)**

400   Unless otherwise specified, all materials were purchased from either Alfa Aesar or Sigma-

401   Aldrich and used as received. The synthesis of CH_3NH_3I was performed using the same

402   previously reported method [31]. The Al_2O_3 (Aldrich, 642991) nanoparticle paste used for

403   characterization measurements was formed by suspending ~ 45 nm particles in a solution of

404   ethanol, terpineol and ethyl cellulose.

405   Glass substrates were cleaned by sonication in ethanol for 10 mins. The mesoporous Al_2O_3

406   layer was formed by drop coating approximately 30 $\mu L/cm^2$ of the nanoparticle solution on

407   the glass substrates, which were then annealed at 500 °C for 30 mins. The perovskite

408   precursor solution was formed by mixing stoichiometric amounts of CH_3NH_3I and PbI_2 in a

409   combination of dimethyl sulfoxide (DMSO) and *N*-methyl-2-pyrrolidone (NMP) (7:3 vol) to

form a (46 wt%) concentration solution. Approximately 30 $\mu L/cm^2$ of the perovskite precursor solution was applied to the surface of the substrate prior to spin-coating. The films were spin-coated using a two-stage process: 1000 rpm for 5 s using an acceleration of 200 rpm/s, then 6000 rpm for 50 s using an acceleration of 6000 rpm/s. A nitrogen gas flow was introduced after 20 s of the second spin-coating step and sustained for a further 20 s. The perovskite films were then annealed on a hot-plate at 100 °C for a duration of 10 mins.

Mixed-cation Mixed-halide Perovskite Sample preparation

The organic cations were purchased from Dyesol; the lead compounds from TCI; Dimethylformamide (DMF), Dimethyl Sulfoxide (DMSO) and cesium iodide from Sigma Aldrich. The mixed cation lead mixed halide perovskite $(Cs_{0.05}(MA_{0.17}FA_{0.83})_{0.95}Pb(I_{0.83}Br_{0.17})_3)$ precursor solutions were prepared by dissolving 1 M FAI, 1.1 M PbI_2, 0.2 M MABr, 0.2 M $PbBr_2$ in a 4:1 (v:v) mixture of anhydrous DMF:DMSO and 1.5 M stock solution of CsI in DMSO was added to the above solution in a 5:95 (CsI:mixture) volume ratio. The perovskite solutions were then spin coated in a two-step program at 1000 and 6000 rpm for 10 and 30 s respectively. During the second step, 50 ul of chlorobenzene was dripped on the spinning substrate 10 s prior to the end. The perovskite film was annealed at 100° C for 30 min.

SEM imaging

The LPC samples were imaged using a Zeiss Merlin high-resolution scanning electron microscope with a beam energy of 3 kV. The SPC, SC and MP samples were imaged using a FEI Nova NanoSEM 450 scanning electron microscope unit with a beam energy of 15 kV.

Magneto-optical measurement

432   The magneto transmission measurements were performed combining long pulse magnetic

433   field meausrements and 150 T short duration pulsed magnets.

434   For the long pulse measurements, the typical duration of the pulse is around 100 ms with the

435   magnetic field up to 66 T. For these measurements, the sample was placed in a liquid helium

436   cryostat. White light from a halogen lamp was used as the excitation source. The light emitted

437   from the lamp was coupled in a 200 µm-diameter multimode fiber, used to illuminate sample.

438   The transmitted light was collected by a 400 µm-diameter multimode fiber and guided to a

439   spectrometer equipped with a liquid nitrogen cooled CCD camera. The typical exposure time

440   was <3 ms, which ensured that the transmission spectra were acquired at an essentially

441   constant magnetic field value.

442   For very high magnetic field measurements (B<150 T), pulse having a typical duration < 10

443   µs were generated by a single turn coil system with a bore diameter of 10 mm. A non-

444   conducting helium-flow cryostat was located in the single turn coil. The sample was kept at a

445   temperature of ~5 K. Magneto-transmission measurements were conducted by a using tunable

446   Opical Parametric Oscillator pumped by a Ti:sapphire laser as the light source. A fast (100

447   MHz) silicon detector and a high speed digital oscilloscope was used for detection.

Reference

1. D. Bi, W. Tress, M. I. Dar, P. Gao, J. Luo, C. Renevier, K. Schenk, A. Abate, F. Giordano, J.-P. Correa Baena, J.-D. Decoppet, S. M. Zakeeruddin, M. K. Nazeeruddin, M. Grätzel and A. Hagfeldt, *Science Advances*, 2016, **2**.

2. M. Saliba, T. Matsui, J.-Y. Seo, K. Domanski, J.-P. Correa-Baena, N. Mohammad K, S. M. Zakeeruddin, W. Tress, A. Abate, A. Hagfeldt and M. Gratzel, *Energy & Environmental Science*, 2016, **9**, 1989-1997.

3. A. Kojima, K. Teshima, Y. Shirai and T. Miyasaka, *Journal of the American Chemical Society*, 2009, **131**, 6050-6051.

4. N. J. Jeon, J. H. Noh, W. S. Yang, Y. C. Kim, S. Ryu, J. Seo and S. I. Seok, *Nature*, 2015, **517**, 476–480.

5. D. P. McMeekin, G. Sadoughi, W. Rehman, G. E. Eperon, M. Saliba, M. T. Hörantner, A. Haghighirad, N. Sakai, L. Korte, B. Rech, M. B. Johnston, L. M. Herz and H. J. Snaith, *Science*, 2016, **351**, 151-155.

6. V. D'Innocenzo, A. R. Srimath Kandada, M. De Bastiani, M. Gandini and A. Petrozza, *Journal of the American Chemical Society*, 2014, **136**, 17730–17733.

7. C. G. Bischak, E. M. Sanehira, J. T. Precht, J. M. Luther and N. S. Ginsberg, *Nano Letters*, 2015, **15**, 4799-4807.

8. Z.-K. Tan, R. S. Moghaddam, M. L. Lai, P. Docampo, R. Higler, F. Deschler, M. Price, A. Sadhanala, L. M. Pazos, D. Credgington, F. Hanusch, T. Bein, H. J. Snaith and R. H. Friend, *Nat Nano*, 2014, **9**, 687-692.

9. M. Saliba, S. M. Wood, J. B. Patel, P. K. Nayak, J. Huang, J. A. Alexander-Webber, B. Wenger, S. D. Stranks, M. T. Hörantner, J. T.-W. Wang, R. J. Nicholas, L. M. Herz, M. B. Johnston, S. M. Morris, H. J. Snaith and M. K. Riede, *Advanced Materials*, 2016, **28**, 923-929.

10. M. A. Green, A. Ho-Baillie and H. J. Snaith, *Nat Photon*, 2014, **8**, 506-514.

11. S. D. Stranks and H. J. Snaith, *Nature Nanotechnology*, 2015, **10**, 391-402.

12. T. Ishihara, *Journal of Luminescence*, 1994, **60-61**, 269–274.

13. M. Hirasawa, T. Ishihara, T. Goto, K. Uchida and N. Miura, *Physica B: Condensed Matter*, 1994, **201**, 427-430.

14. M. Hirasawa, T. Ishihara and T. Goto, *Journal of the Physical Society of Japan*, 1994, **63**, 3870-3879.

15. M. E. Ziffer, J. C. Mohammed and D. S. Ginger, *ACS Photonics*, 2016, **3**, 1060–1068.

16. K. Galkowski, A. Mitioglu, a. miyata, p. plochocka, o. Portugall, G. E. Eperon, J. T.-W. Wang, T. Stergiopoulos, S. D. Stranks, H. Snaith and R. J. Nicholas, *Energy & Environmental Science*, 2016, **9**, 962-970.

17. A. Miyata, A. Mitioglu, P. Plochocka, O. Portugall, J. T.-W. Wang, S. D. Stranks, H. J. Snaith and R. J. Nicholas, *Nat Phys*, 2015, **11**, 582–587.

18. A. M. Soufiani, F. Huang, P. Reece, R. Sheng, A. Ho-Baillie and M. A. Green, *Applied Physics Letters*, 2015, **107**, 231902.

19. Y. Fu, H. Zhu, C. C. Stoumpos, Q. Ding, J. Wang, M. G. Kanatzidis, X. Zhu and S. Jin, *ACS Nano*, 2016, **10**, 7963-7972.

20. S. A. March, D. B. Riley, C. Clegg, D. Webber, X. Liu, M. Dobrowolska, J. K. Furdyna, I. G. Hill and K. C. Hall, *arXiv preprint arXiv:1602.05186*, 2016.

21. A. R. Srimath Kandada and A. Petrozza, *Accounts of Chemical Research*, 2016, **49**, 536–544.

22. G. Grancini, A. R. Srimath Kandada, J. M. Frost, A. J. Barker, M. De Bastiani, M. Gandini, S. Marras, G. Lanzani, A. Walsh and A. Petrozza, *Nat Photon*, 2015, **9**, 695-701.

23. Q. Lin, A. Armin, R. C. R. Nagiri, P. L. Burn and P. Meredith, *Nature Photonics*, 2014, **9**, 106–112.

24. J. Even, L. Pedesseau and C. Katan, *The Journal of Physical Chemistry C*, 2014, **118**, 11566–11572.

25. V. D'Innocenzo, G. Grancini, M. J. P. Alcocer, A. R. S. Kandada, S. D. Stranks, M. M. Lee, G. Lanzani, H. J. Snaith and A. Petrozza, *Nat Commun*, 2014, **5**.

26. L. M. Herz, *Annual Review of Physical Chemistry*, 2016, **67**, 65-89.

27. J. Kim, J. S. Yun, X. Wen, A. M. Soufiani, C. F. J. Lau, B. Wilkinson, J. Seidel, M. A. Green, S. Huang and A. W. Y. Ho-Baillie, *The Journal of Physical Chemistry C*, 2016, **120**, 11262–11267.

28. J. Burschka, N. Pellet, S.-J. Moon, R. Humphry-Baker, P. Gao, M. K. Nazeeruddin and M. Gratzel, *Nature*, 2013, **499**, 316-319.

29. W. S. Yang, J. H. Noh, N. J. Jeon, Y. C. Kim, S. Ryu, J. Seo and S. I. Seok, *Science*, 2015, **348**, 1234-1237.

30. M. Liu, M. B. Johnston and H. J. Snaith, *Nature*, 2013, **501**, 395-398.

31. F. Huang, Y. Dkhissi, W. Huang, M. Xiao, I. Benesperi, S. Rubanov, Y. Zhu, X. Lin, L. Jiang and Y. Zhou, *Nano Energy*, 2014, **10**, 10-18.

32. W. Zhang, S. Pathak, N. Sakai, T. Stergiopoulos, P. K. Nayak, N. K. Noel, A. A. Haghighirad, V. M. Burlakov, D. W. deQuilettes, A. Sadhanala, W. Li, L. Wang, D. S. Ginger, R. H. Friend and H. J. Snaith, *Nat Commun*, 2015, **6**.

33. C. F. Klingshirn, *Semiconductor optics*, Springer, 2007.

34. J. Tilchin, D. N. Dirin, G. I. Maikov, A. Sashchiuk, M. V. Kovalenko and E. Lifshitz, *ACS Nano*, 2016, **10**, 6363-6371.

35. P. C. Makado and N. C. McGill, *Journal of Physics C: Solid State Physics*, 1986, **19**, 873.

36. G. Mahan, *Proc. 1971 Antwerp Advanced Study Inst*, 1972.

37. D. Li, G. Wang, H.-C. Cheng, C.-Y. Chen, H. Wu, Y. Liu, Y. Huang and X. Duan, *Nat Commun*, 2016, **7**.

38. A. Osherov, E. M. Hutter, K. Galkowski, R. Brenes, D. K. Maude, R. J. Nicholas, P. Plochocka, V. Bulović, T. J. Savenije and S. D. Stranks, *Advanced Materials*, 2016, **28**, 10757-10763.

39. K. Galkowski, A. A. Mitioglu, A. Surrente, Z. Yang, D. K. Maude, P. Kossacki, G. E. Eperon, J. T. W. Wang, H. J. Snaith, P. Plochocka and R. J. Nicholas, *Nanoscale*, 2017, **9**, 3222.

40. M. R. Filip, G. E. Eperon, H. J. Snaith and F. Giustino, *Nature communications*, 2014, **5**.

41. M. A. Pérez-Osorio, R. L. Milot, M. R. Filip, J. B. Patel, L. M. Herz, M. B. Johnston and F. Giustino, *The Journal of Physical Chemistry C*, 2015, **119**, 25703-25718.

42. A. M. A. Leguy, A. R. Goni, J. M. Frost, J. Skelton, F. Brivio, X. Rodriguez-Martinez, O. J. Weber, A. Pallipurath, M. I. Alonso, M. Campoy-Quiles, M. T. Weller, J. Nelson, A. Walsh and P. R. F. Barnes, *Physical Chemistry Chemical Physics*, 2016, **18**, 27051-27066.

43. Y. Yamada, T. Nakamura, M. Endo, A. Wakamiya and Y. Kanemitsu, *IEEE Journal of Photovoltaics*.

44. C. Motta, P. Mandal and S. Sanvito, *Physical Review B*, 2016, **94**, 045202.

45. M. B. Price, J. Butkus, T. C. Jellicoe, A. Sadhanala, A. Briane, J. E. Halpert, K. Broch, J. M. Hodgkiss, R. H. Friend and F. Deschler, *Nature Communications*, 2015, **6**.

46. Y. Yang, D. P. Ostrowski, R. M. France, K. Zhu, J. van de Lagemaat, J. M. Luther and M. C. Beard, *Nat Photon*, 2015, **10**, 53–59.

47. N. Sestu, M. Cadelano, V. Sarritzu, F. Chen, D. Marongiu, R. Piras, M. Mainas, F. Quochi, M. Saba, A. Mura and G. Bongiovanni, *The Journal of Physical Chemistry Letters*, 2015, **6**, 4566-4572.